Vibration Compensation Control of BPMSM With Dead-Time Effect Based on Adaptive Neural Network Band-Pass Filter

Xin Wang and Huangqiu Zhu, *Member, IEEE*

***Abstract*—In order to solve the problem of rotor vibration for the bearingless permanent magnet synchronous motor, a vibration compensation control method based on adaptive neural network band-pass filter (ANNBPF) is proposed. First, the mechanism of rotor vibration is obtained by theoretical analysis. Second, the ANNBPF is used to extract the components related to the frequency of the unbalanced vibration and the dead-time (DT) vibration to realize the vibration compensation control. Additionally, the DT effect is compensated by detecting the current polarity to improve the compensation effect. Finally, a vibration compensation control system based on ANNBPF and current polarity detection is constructed.**

***Index Terms*—Adaptive neural network band-pass filter (ANNBPF), bearingless permanent magnet synchronous motor (BPMSM), dead-time (DT) effect, vibration compensation.**

I. Introduction

THE permanent magnet synchronous motor (PMSM) has the advantages of high efficiency, high power factor, small size, and light weight. However, when the PMSM with mechanical bearings is running at high speed, friction and wear will occur between the bearings and the motor, which not only reduce the efficiency and life of motor but also increase the number of motors maintenance. On the other hand, in some extreme conditions, such as chemical, pharmaceutical, biomedicine, semiconductor, etc., mechanical bearings cannot be used due to the requirements of ultrahigh cleanliness. In order to solve the problem effectively, the bearingless PMSMs (BPMSMs) have the advantages of no mechanical friction and wear, no lubrication, no sealing, low power consumption, high critical speed, etc., which can be applied in special fields [1]–[4]. The rotor of the BPMSM will produce inaccuracies and tolerance variations in the process of mechanical manufacturing; therefore, the rotor vibration is inevitable. In order to suppress the rotor vibration, it is necessary to carry out vibration compensation control.

The vibration compensation control plays an important role in the stable operation of the BPMSM system. Plentiful scholars have conducted research on this aspect [5]–[10]. The unbalance of rotor mass is one of the causes of the rotor vibration of the BPMSM in high speed application. Numerous research articles have explored this aspect and proposed different methods for vibration compensation control. In [5], the problem of rotor vibration when the center of mass is unbalanced is analyzed, the mathematical model of the inertia center is derived, and the synchronous vibration displacement signal is extracted to realize the vibration compensation control. In [6]–[8], the amplitude of displacement signal related to vibration is extracted by different methods, and the adjusted compensation signal is injected into the forward channel to complete the vibration compensation control. At the same time, these pieces of literature also use the inverse system to improve the control effect. Applying the neural network structure with strong fitting and approximation ability to the inverse system will achieve better vibration control effect [11]–[14]. In [9], the reason of vibration caused by unbalanced mass is analyzed, and a control strategy combining unbalance feedforward compensation with current compensation is proposed to realize vibration compensation control. In [10], the rotor position and vibration displacement can be estimated by extended Kalman filter (EKF). Although the EKF can compensate for the vibration, the computational complexity of the EKF is too large, which is unfavorable to the real-time control. These methods can improve the vibration problem caused by mass unbalance. However, these researches are only aimed at the unbalance of the mass, and cannot fully compensate the rotor rotation. Through theoretical analysis, it is founded that the dead-time (DT) effect can also cause the vibration of the rotor. DT effect is particularly obvious when BPMSM is running at low speed. Therefore, for the low-speed applications of BPMSM [15], [16], the vibration caused by DT effect will seriously affect its performance.

DT is an essential part in the control of the BPMSM, which will not only reduce the efficiency of the whole control system, but also make the control effect worse. The DT effect will increase the high-order harmonic currents of torque and suspension force windings in the BPMSM, and cause rotor vibration. Therefore, accurate DT compensation (DTC) can effectively suppress the rotor vibration of the BPMSM. DTC control is

Manuscript received June 22, 2021; revised October 15, 2021 and December 2, 2021; accepted December 31, 2021. Date of publication January 10, 2022; date of current version February 18, 2022. This work was supported in part by the National Natural Science Foundation of China under Grant 61973144 and in part by the Priority Academic Program Development of Jiangsu Higher Education Institutions under Grant PAPD-2018-87. Recommended for publication by Associate Editor J. He. *(Corresponding author: Huangqiu Zhu.)*

The authors are with the School of Electrical and Information Engineering, Jiangsu University, Zhenjiang 212013, China (e-mail: 2111907009@stmail.ujs.edu.cn; zhuhuangqiu@ujs.edu.cn).

Color versions of one or more figures in this article are available at https://doi.org/10.1109/TPEL.2022.3141454.

Digital Object Identifier 10.1109/TPEL.2022.3141454

widely researched in PMSM [17]–[23]. In [17], the harmonic and disturbance of current is reduced by revised repetitive controller (RRC) to achieve better DTC effect. However, it's difficult to adjust the stability of RRC, which needs more consideration in practical application. In [18] and [19], the influence of DT effect on motor current and voltage harmonics is analyzed, and the adaptive controller is used to compensate these bad effects. This method can realize the DTC control well. In [20] and [21], the adaptive method is used for DTC, in which Liu and Zhu [20] directly observed and compensated the DT voltage in the system online through the adaptive method. While Wang *et al.* [21] not only analyzed the disturbance voltage caused by the nonlinear factors of the inverter but also analyzed the harmonic influence caused by the back EMF harmonic. In [22], a current boundary is set up for the voltage error compensation near zero current in the DTC control of current polarity detection. This method has good control effect and has certain value in practical application. In [23], the neutral point potential and terminal voltage potential are sampled to realize the accurate judgment of current polarity. However, due to the cost consideration, too many voltage sensors will not be installed. Therefore, in practical application, it is necessary to obtain accurate voltage value without sensor.

In order to solve the vibration problem of the BPMSM rotor caused by the unbalance of the mass and DT effect, the influences of unbalance vibration and DT vibration are analyzed in detail. A vibration compensation control method of the BPMSM based on adaptive neural network band-pass filter (ANNBPF) is proposed. First, the influence of DT effect on BPMSM rotor vibration is analyzed. And, the correctness of the analysis is verified by theoretical analysis and experimental analysis. Then, the ANNBPFs are used to extract the harmonic displacement components and harmonic current components, and the compensation signals are injected into the forward channel to complete the compensation control. Finally, the current components extracted by the ANNBPFs are sent to the current polarity detection method to realize the DTC control, so as to avoid the problem of false compensation at zero current and further improve the performance of the control system.

The rest of this article is organized as follows. In Section II, the vibration mechanism and analysis of BPMSM are briefly summarized. In Section III, the vibration compensation control strategies of BPMSM are delivered. In Section IV, the correctness and effectiveness of the vibration compensation control method are verified on the experimental platform. Finally, Section V concludes this article.

II. Vibration Mechanism Analysis of the BPMSM

A. Mathematical Model of Suspension Force

For the BPMSM, when the difference between the pole pair numbers of the torque windings (P_{M}) and the pole pair numbers of the suspension force windings (P_{B}) is 1, and the current frequency of torque windings (ω_{M}) is equal to that of suspension force windings (ω_{B}), i.e., $P_{\mathrm{M}} = P_{\mathrm{B}} \pm 1$ and $\omega_{\mathrm{M}} = \omega_{\mathrm{B}}$, the BPMSM will be able to operate stably [24]–[26]. The suspension force formula can be expressed as [27], [28]

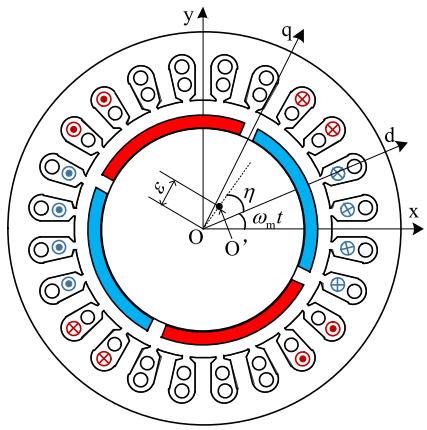

Fig. 1. Unbalance vibration diagram of rotor.

$$\begin{bmatrix} F_{\mathrm{x}} \\ F_{\mathrm{y}} \end{bmatrix} = (K_{\mathrm{M}} + K_{\mathrm{L}}) \begin{bmatrix} \psi_{\mathrm{Md}} & \psi_{\mathrm{Mq}} \\ -\psi_{\mathrm{Mq}} & \psi_{\mathrm{Md}} \end{bmatrix} \begin{bmatrix} i_{\mathrm{Bd}} \\ i_{\mathrm{Bq}} \end{bmatrix} + K_{\mathrm{ecc}} \begin{bmatrix} x \\ y \end{bmatrix} \tag{1}$$

where ψ_{Md} and ψ_{Mq} are the flux linkages of torque windings in d–q rotating coordinate system, respectively, $\psi_{\mathrm{Md}} = L_{\mathrm{Md}}(i_{\mathrm{Md}} + I_{\mathrm{f}})$, $\psi_{\mathrm{Mq}} = L_{\mathrm{Mq}} i_{\mathrm{Mq}}$, i_{Md} and i_{Mq} are the currents of d–q-axis of torque windings, respectively, L_{Md} and L_{Mq} are the self-inductances of d–q-axis of torque windings, respectively, I_{f} is the equivalent excitation current of permanent magnet, i_{Bd} and i_{Bq} are the currents of d–q-axis of suspension force windings, respectively, x and y are displacements in stationary coordinate system, respectively, F_{x} and F_{y} are suspension forces in stationary coordinate system, respectively, K_{M} and K_{L} are Maxwell forces and Lorentz forces constants, respectively [24], and K_{ecc} is the force-displacement stiffness [27], [28].

B. Mechanism Analysis of Unbalanced Vibration

During the operation of the BPMSM, there are many factors that cause rotor vibration, such as the error in the machining process of the rotor and the DT effect, which will be studied in this article. The rotor machining error mainly causes the unbalance of the mass, which belongs to the mechanical unbalance of the rotating system and will cause the unbalance vibration of the rotor. A brief schematic diagram of unbalanced vibration is shown in Fig. 1. When the rotor mass is unbalanced, the geometric center O of the rotor will not coincide with the mass center O′. The distance between these two points is defined as ε. And, the line segment formed by these two points is shown as a dotted line in Fig. 1. The angle between the dotted line segment and the d-axis of the rotating coordinate system is η. When the rotor rotates at the mechanical angular speed ω_{m}, the angle between the dotted line segment and the x-axis in the stationary coordinate system of the suspension force windings is $\eta + \omega_{\mathrm{m}} t$. Due to the unbalanced motion of the rotor, the periodic unbalance force is F_a. The component force of the F_a in the x–y

coordinate system can be expressed as [5], [6]

$$\begin{cases} F_{ax} &= m\varepsilon\omega_{\mathrm{m}}^2 \cos(\omega_{\mathrm{m}} t + \eta) \\ F_{ay} &= m\varepsilon\omega_{\mathrm{m}}^2 \sin(\omega_{\mathrm{m}} t + \eta) \end{cases} \tag{2}$$

where F_{ax} and F_{ay} are the components of the unbalanced force F_a in the x- and y-direction, respectively, m is the mass of the rotor, ε is the distance between the geometric center and the mass center of the rotor, and ω_{m} is the mechanical angular velocity.

Suppose x_a and y_a are unbalanced vibration displacement components along the x- and y-direction. In view of the symmetry of motor structure, the control stiffness of unbalanced vibration displacement along x-direction equals to that along y-direction, thus, the unbalanced vibration displacement excited by unbalanced exciting force F_a can be expressed as follows:

$$\begin{cases} x_a = A\cos(\omega_{\mathrm{m}} t + \eta - \gamma) \\ y_a = A\sin(\omega_{\mathrm{m}} t + \eta - \gamma) \end{cases} \tag{3}$$

where γ is the phase lag of the unbalanced vibration displacement relative to the unbalanced exciting force and A is the amplitude of unbalanced vibration displacement component.

According to (2) and (3), the periodic unbalance displacement and unbalance force will run at the angular velocity ω_{m} due to the existence of unbalanced vibration, and their vibration amplitude is A and $m\varepsilon\omega_{\mathrm{m}}^2$. In order to compensate the unbalanced vibration, it is necessary to obtain the amplitude of the displacement and the force with the same frequency as the angular velocity ω_{m}, and then carry out the feedforward compensation control.

C. Mechanism Analysis of DT Effect Vibration

The unbalanced force generated during the operation of the BPMSM is not only affected by the manufacture of the motor, but also by the control process. Among them, the DT effect is the most direct reason. DT effect is caused by the introduction of DT, which avoid the short circuit of the upper and lower arms of the inverter.

In order to simplify the analysis, take the A-phase bridge arm of the three-phase bridge voltage source inverter unit as an example to analyze the influence of the DT effect on the inverter. Fig. 2 is a schematic diagram of the topological structure of the A-phase bridge arm in the inverter unit. It is stipulated that the direction of current flowing from the power device to the motor is the positive direction, denoted as $i > 0$, otherwise $i < 0$ [29].

The dotted line in Fig. 2 represents the ideal voltage waveform, and the solid line represents the actual voltage waveform. Fig. 2(a) shows the voltage waveform when $i > 0$, and Fig. 2(b) shows the voltage waveform when $i < 0$. Where u_{dc}, u_{SW}, and u_{D} are the dc bus voltage, switching device, and diode voltage drop, respectively, and T_{r}, T_{f}, T_{on}, T_{off}, and T_{PWM} are the ON and OFF delay time, high-level and low-level time, and switching cycle, respectively.

For surface-mounted PMSM without flux weakening control, the phase voltage change caused by DT voltage is transformed into voltage in two-phase rotating coordinate system by Clarke and Park transform [18]–[20]. When only the main components

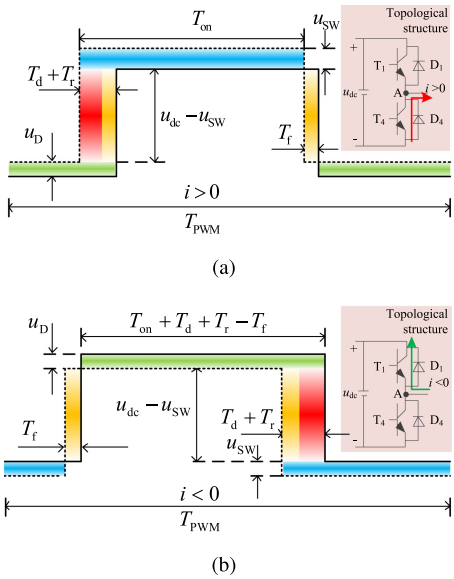

Fig. 2. Topological structure of A-phase bridge arm and ideal and actual voltage waveform. (a) $i > 0$. (b) $i < 0$.

in the Fourier series are considered, it can be expressed as [18]

$$\begin{bmatrix} \Delta u_{\mathrm{d}} \\ \Delta u_{\mathrm{q}} \end{bmatrix} = \begin{bmatrix} -\frac{48}{35\pi}\Delta u_{\mathrm{dead}} \sin(6\theta_{\mathrm{e}}) \\ \frac{4}{\pi}\Delta u_{\mathrm{dead}} - \frac{8}{35\pi}\Delta u_{\mathrm{dead}} \cos(6\theta_{\mathrm{e}}) \end{bmatrix} \tag{4}$$

where Δu_{dead} is the error voltage caused by DT effect, Δu_{d} is the d-axis error voltage, Δu_{q} is the q-axis error voltage, and θ_{e} is the electrical angle.

When the motor is regarded as resistance and inductance load, the currents of d–q-axis can be expressed as [18]

$$\begin{bmatrix} \Delta i_{\mathrm{d}} \\ \Delta i_{\mathrm{q}} \end{bmatrix} = -\frac{4\Delta u_{\mathrm{dead}}}{\pi} \begin{bmatrix} \frac{12\sin(6\omega_{\mathrm{e}} t - \phi_{\mathrm{d6}})}{35 Z_{\mathrm{d6}}} \\ -\frac{1}{R_{\mathrm{s}}} + \frac{2\cos(6\omega_{\mathrm{e}} t - \phi_{\mathrm{q6}})}{35 Z_{\mathrm{q6}}} \end{bmatrix} \tag{5}$$

where ω_{e} is the electric angular velocity and $\omega_{\mathrm{e}} = \omega_{\mathrm{M}} = \omega_{\mathrm{B}}$, the impedance and phase angle are

$$\begin{cases} Z_{jk} &= \sqrt{R_{\mathrm{s}}^2 + (k\omega_{\mathrm{e}} L_j)^2}, \ j = \mathrm{d}, \mathrm{q} \\ \phi_{jk} &= \arctan\frac{k\omega_{\mathrm{e}} L_j}{R_{\mathrm{s}}}, \quad k = 6. \end{cases}$$

For the BPMSM, (5) can be expressed by Δi_{Md} and Δi_{Mq} for d- and q-axis currents increment of torque windings and Δi_{Bd} and Δi_{Bq} for suspension force windings, respectively. As a result of the second part on the right-hand side of the equal sign in (1) has been compensated by feedforward control, and the displacement is small in actual operation, the second part can be ignored in the analysis process. Taking the surface-mounted BPMSM as an example, namely $L_{\mathrm{Md}} = L_{\mathrm{Mq}}$, after substituting the corresponding current into (1), the vibration force caused by DT effect can be expressed as

$$\begin{bmatrix} \Delta F_{\mathrm{x}} \\ \Delta F_{\mathrm{y}} \end{bmatrix} = K_{\mathrm{cur}} \begin{bmatrix} \Delta i_{\mathrm{Md}} + I_{\mathrm{f}} & \Delta i_{\mathrm{Mq}} \\ -\Delta i_{\mathrm{Mq}} & \Delta i_{\mathrm{Md}} + I_{\mathrm{f}} \end{bmatrix} \begin{bmatrix} \Delta i_{\mathrm{Bd}} \\ \Delta i_{\mathrm{Bq}} \end{bmatrix} \tag{6}$$

where K_{cur} is the force current stiffness.

After substituting the corresponding current in (5) into (6), and taking the suspension force in the x-direction as an example, the

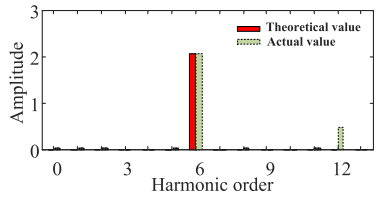

Fig. 3. Harmonic analysis of vibration force.

incremental expression for the vibration of the suspension force in the x-direction can be obtained as

$$\begin{aligned}\Delta F_{\mathrm{x}} &= K_{\mathrm{cur}}\left[(\Delta i_{\mathrm{Md}} + I_{\mathrm{f}})\cdot\Delta i_{\mathrm{Bd}} + \Delta i_{\mathrm{Mq}}\cdot\Delta i_{\mathrm{Bq}}\right] \\ &= K_{\mathrm{cur}}\left[\Delta i_{\mathrm{Md}}\cdot\Delta i_{\mathrm{Bd}} + \Delta i_{\mathrm{Mq}}\cdot\Delta i_{\mathrm{Bq}} + I_{\mathrm{f}}\cdot\Delta i_{\mathrm{Bd}}\right] \\ &= K_{\mathrm{cur}}\frac{16\Delta u_{\mathrm{dead}}^2}{35^2\pi^2}\left\{\begin{bmatrix}\frac{12\sin(6\omega_{\mathrm{e}}t-\phi_{\mathrm{Md6}})}{Z_{\mathrm{Md6}}}\end{bmatrix}\cdot\right. \\ &\quad\left.\begin{bmatrix}\frac{12\sin(6\omega_{\mathrm{e}}t-\phi_{\mathrm{Bd6}})}{Z_{\mathrm{Bd6}}}\end{bmatrix} + \begin{bmatrix}\frac{2\cos(6\omega_{\mathrm{e}}t-\phi_{\mathrm{Mq6}})}{Z_{\mathrm{Mq6}}}\end{bmatrix}\cdot\begin{bmatrix}\frac{2\cos(6\omega_{\mathrm{e}}t-\phi_{\mathrm{Bq6}})}{Z_{\mathrm{Bq6}}}\end{bmatrix}\right\} \\ &\quad + K_{\mathrm{cur}}I_{\mathrm{f}}\left\{-\frac{4\Delta u_{\mathrm{dead}}}{\pi}\left[\frac{12\sin(6\omega_{\mathrm{e}}t-\phi_{\mathrm{Bd6}})}{35Z_{\mathrm{Bd6}}}\right]\right\} \\ &= K_{\mathrm{cur}}\frac{4\Delta u_{\mathrm{dead}}}{\pi}\left[\frac{16\Delta u_{\mathrm{dead}}}{35^2\pi}(\Delta F_{\mathrm{x1}}+\Delta F_{\mathrm{x2}}) - \Delta F_{\mathrm{x3}}\right]\end{aligned} \tag{7}$$

where

$$\Delta F_{\mathrm{x1}} = 36\sin(6\omega_{\mathrm{e}}t-\phi_{\mathrm{Md6}})\cdot\sin(6\omega_{\mathrm{e}}t-\phi_{\mathrm{Bd6}})/(Z_{\mathrm{Md6}}\cdot Z_{\mathrm{Bd6}})$$

$$\Delta F_{\mathrm{x2}} = \cos(6\omega_{\mathrm{e}}t-\phi_{\mathrm{Mq6}})\cdot\cos(6\omega_{\mathrm{e}}t-\phi_{\mathrm{Bq6}})/(Z_{\mathrm{Mq6}}\cdot Z_{\mathrm{Bq6}})$$

$$\Delta F_{\mathrm{x3}} = 12I_{\mathrm{f}}\sin(6\omega_{\mathrm{e}}t-\phi_{\mathrm{Bd6}})/(35Z_{\mathrm{Bd6}}).$$

According to the trigonometric function formula, the correlation coefficient of electrical angle velocity ω_{e} with ΔF_{x1} and ΔF_{x2} is 12, while that of ω_{e} and ΔF_{x3} is 6, and the process of ΔF_{y} is similar to the ΔF_{x}. Therefore, it can be inferred that due to the DT effect, there will be 6th and 12th harmonic components related to the electrical angular velocity in the vibration force.

Taking $\omega_{\mathrm{e}} = 314$, $K_{\mathrm{cur}} = 1.338$, $I_{\mathrm{f}} = 12.295$, and $\Delta u_{\mathrm{dead}} = 6.2$ as an example, the force-harmonic diagram as shown in Fig. 3 can be drawn, and compared with the results obtained in actual working conditions, it can be found that in (7), the amplitude of the sixth harmonic is the main influencing factor, and the waveform tested in practice is consistent with the theoretical analysis. However, the theoretical amplitude of the 12th harmonic is very small, and there is a difference between the 12th harmonic and the theoretical value in the actual working condition, which may be related to the unmodeled nonlinear factor of the inverter. Therefore, in practice, the harmonic order of the force caused by the DT effect is mainly 6th and 12th.

III. Proposed Vibration Compensation Control Method

A. Unbalanced Vibration Compensation Control

According to the above-mentioned analysis, the main vibration sources of the BPMSM are the unbalance of rotor mass and DT effect in control. Between them, the vibration force caused by unbalanced mass is mainly the same frequency with mechanical angular velocity ω_{m}, and the vibration force caused by DT effect is mainly the 6th and 12th harmonic components related to electrical angular velocity ω_{e}. In order to compensate and control these vibration forces, it is necessary to obtain the amplitude related to the frequency of these vibration forces.

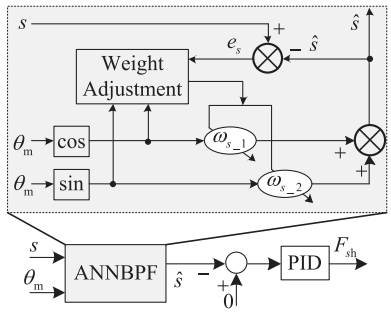

Fig. 4. Basic structure of the displacement ANNBPF.

It can be seen from (2) that when the operating speed of the unbalanced force F_a is ω_{m}, the amplitude of F_a changes squarely with the increase of the speed. Hence, the higher the rotor speed, the larger the amplitude of the unbalanced force. It is relatively difficult to extract the unbalanced force, but the rotor displacement detection is much simpler. Therefore, how to extract the amplitude of displacement with the same frequency is the key to realize vibration compensation.

ANNBPF is an adaptive filter. It cannot only extract the amplitude of harmonic signal with the same frequency as the speed, but also has a fast convergence speed. Therefore, the use of ANNBPF is a better choice. The basic structure of the ANNBPF in the x- and y-direction is shown in Fig. 4. And, the formula for extracting harmonic displacement is

$$\begin{cases}\hat{x} = \omega_{x\_1}\cos\theta_{\mathrm{m}} + \omega_{x\_2}\sin\theta_{\mathrm{m}} \\ \hat{y} = \omega_{y\_1}\cos\theta_{\mathrm{m}} + \omega_{y\_2}\sin\theta_{\mathrm{m}}\end{cases} \tag{8}$$

where ω_{x_1}, ω_{x_2}, ω_{y_1}, and ω_{y_2} are the cosine component weight amplitudes and sinusoidal component weight amplitudes of displacement harmonic in the x- and y-direction, respectively. $\hat{x}$ and $\hat{y}$ are the amplitudes of displacement harmonic component in x- and y-direction, respectively.

The least mean square algorithm with small amount of calculation and fast convergence speed can be used to adjust the weights, and the cost function is defined as

$$J = (x-\hat{x})^2 + (y-\hat{y})^2 = e_{\mathrm{x}}^2 + e_{\mathrm{y}}^2 \tag{9}$$

where x and y are the displacement sampling values and e_{x} and e_{y} are the displacement errors.

In Fig. 4, s and θ_{m} are taken as the inputs of the displacement ANNBPF and the output variable is $\hat{s}$, where s refers to the displacement in x- and y-direction, i.e., $s = x, y$. The error signal e_s is obtained by the difference between the input variable s and the output variable $\hat{s}$ of the displacement ANNBPF. The adjusted weights ω_{s_1} and ω_{s_2} can be obtained by taking the sine and cosine values of θ_{m} and the error signals e_s as the

inputs of the weight adjustment module. The least mean square algorithm with low complexity, small amount of calculation, and fast convergence speed is used to adjust the weights online, the adjustment formula can be expressed as [18]

$$\begin{cases} \omega_{s\_1}(k+1) &= \omega_{s\_1}(k) + 2\mu_1 e_s \cos\theta_{\rm m} \\ \omega_{s\_2}(k+1) &= \omega_{s\_2}(k) + 2\mu_1 e_s \sin\theta_{\rm m} \end{cases},\ s = x, y \quad (10)$$

where ω_{s_1} and ω_{s_2} are the weights of the neuron in the *k*th sampling period, ω_{s_1} is refer to ω_{x_1} and ω_{y_1}, ω_{s_2} is refer to ω_{x_2} and ω_{y_2}, μ_1 is the learning rate, and e_s is the difference between the input variable s and the output variable $\hat{s}$ of the ANNBPF, the e_s is refer to e_x and e_y.

In order to prove the stability of (10) and give the value range of the learning rate μ_1. First, find the expected values on both sides of (10) as

$$E[\boldsymbol{\omega}_s(k+1)] = E[\boldsymbol{\omega}_s(k)] + 2\mu_1 E[e_s \cdot \boldsymbol{r}_{\rm m}(k)] \quad (11)$$

where $\boldsymbol{\omega}_s$ is $[\omega_{s\_1}, \omega_{s\_1}]^{\rm T}$ and $\boldsymbol{r}_{\rm m}$ is $[\cos\theta_{\rm m}, \sin\theta_{\rm m}]^{\rm T}$.

Since $\boldsymbol{\omega}_s$ and $\boldsymbol{r}_{\rm m}$ are independent of each other, (11) can be rewritten as

$$\begin{aligned} E[\boldsymbol{\omega}_s(k+1)] &= E[\boldsymbol{\omega}_s(k)] + 2\mu_1 \{\boldsymbol{H} - \boldsymbol{R}E[\boldsymbol{\omega}_s(k)]\} \\ &= (\boldsymbol{I} - 2\mu_1 \boldsymbol{R}) E[\boldsymbol{\omega}_s(k)] + 2\mu_1 \boldsymbol{H} \end{aligned} \quad (12)$$

where $\boldsymbol{I}$ is the unit matrix, $\boldsymbol{H} = E[x \cdot \boldsymbol{r}_{\rm m}]$, and $\boldsymbol{R} = E[\boldsymbol{r}_{\rm m}(k) \cdot \boldsymbol{r}_{\rm m}^{\rm T}(k)]$.

The system will be stable when all the eigenvalues of the matrix $[\boldsymbol{I} - 2\mu_1 \boldsymbol{R}]$ fall inside the circle. Let the eigenvalue of $\boldsymbol{R}$ be λ_i and the eigenvalue of the matrix $[\boldsymbol{I} - 2\mu_1 \boldsymbol{R}]$ is $(1 - 2\mu_1\lambda_i)$. At this time, it is need to ensure that the eigenvalue $|1 - 2\mu_1\lambda_i| < 1$, then the system shown in (12) is stable and the learning rate $0 < \mu_1 < 1/\lambda_i$ is obtained. When λ_i takes the maximum value of $\lambda_{\rm max1}$, the system will be in a stable state, and the matrix is related to $\cos\theta_{\rm m}$ and $\sin\theta_{\rm m}$.

Through the displacement ANNBPF, the amplitude of the same frequency signal as $\omega_{\rm m}$ in the displacements x and y can be extracted. After that 0 can be used as the target command to make difference with the extracted vibration displacements $\hat{x}$ and $\hat{y}$, and the compensated control forces $F_{\rm xh}$ and $F_{\rm yh}$ can be obtained by adjusting the results by PID controller. The control implementation block diagram is shown in Fig. 4.

B. DT Effect Vibration Compensation Control

The introduction of DT occurs not only in torque control but also in suspension force control. According to (6) and (7), the vibration force caused by the DT effect mainly exists in the form of the 6th and 12th harmonics of the electrical angular velocity. Therefore, only the amplitudes of the 6th and 12th harmonics need to be extracted to realize the vibration compensation control caused by the DT effect. Here, the ANNBPF in Section III-A is also used to extract the harmonics in the *d*- and *q*-axis currents. The basic structure of the ANNBPF for *d*–*q*-axis currents is shown in Fig. 5. And, the formula for extracting harmonic current is

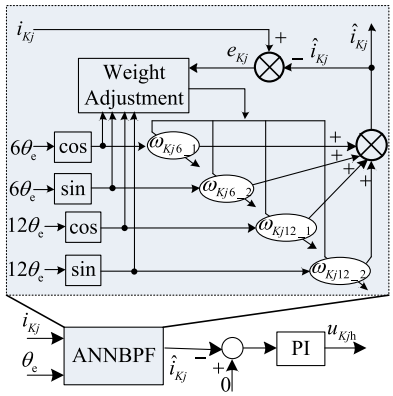

Fig. 5. Basic structure of the DT ANNBPF.

$$\begin{cases} \hat{i}_{\rm Kd} = \omega_{\rm Kd6\_1}\cos(6\theta_{\rm e}) + \omega_{\rm Kd6\_2}\sin(6\theta_{\rm e}) \\ +\omega_{\rm Kd12\_1}\cos(12\theta_{\rm e}) + \omega_{\rm Kd12\_2}\sin(12\theta_{\rm e}) \\ \hat{i}_{\rm Kq} = \omega_{\rm Kq6\_1}\cos(6\theta_{\rm e}) + \omega_{\rm Kq6\_2}\sin(6\theta_{\rm e}) \\ +\omega_{\rm Kq12\_1}\cos(12\theta_{\rm e}) + \omega_{\rm Kq12\_2}\sin(12\theta_{\rm e}) \end{cases},\quad K = {\rm M}, {\rm B}. \quad (13)$$

In Fig. 5, K is used to represent M and B, and j is used to represent *d* and *q*. Therefore, there are four combinations of i_{Kj} in Fig. 5, which are the *d*- and *q*-axis currents $i_{\rm Md}$ and $i_{\rm Mq}$ of the torque windings, respectively, and the *d*- and *q*-axis currents of the suspension force windings $i_{\rm Bd}$ and $i_{\rm Bq}$, respectively. e_{Kj}, $\hat{i}_{Kj}$, ω_{Kj6_1}, ω_{Kj6_2}, ω_{Kj12_1}, and ω_{Kj12_2} are the same as i_{Kj}. i_{Kj} and $\theta_{\rm e}$ are used as the input of the *d*–*q*-axis current ANNBPF, respectively, and $\hat{i}_{Kj}$ is used as the output of the ANNBPF. The error signal e_{Kj} obtained by the difference between i_{Kj} and $\hat{i}_{Kj}$, and the adjusted weight values ω_{Kj6_1}, ω_{Kj6_2}, ω_{Kj12_1}, and ω_{Kj12_2} can be obtained by taking error signal e_{Kj} and the sine and cosine values of $6\theta_{\rm e}$ and $12\theta_{\rm e}$ as the input of the weight adjustment module. The adjustment formula can be expressed as [18]

$$\begin{cases} \omega_{Kjv\_1}(k+1) = \omega_{Kjv\_1}(k) \\ \qquad\qquad + 2\mu_2 e_{Kj}\cos(v\theta_{\rm e}) \\ \omega_{Kjv\_2}(k+1) = \omega_{Kjv\_2}(k) \\ \qquad\qquad + 2\mu_2 e_{Kj}\sin(v\theta_{\rm e}) \end{cases}, \begin{matrix} v = 6, 12 \\ K = {\rm M}, {\rm B} \\ j = {\rm d}, {\rm q} \end{matrix} \quad (14)$$

where $\omega_{Kjv\_1}(k)$ and $\omega_{Kjv\_2}(k)$ are the weights of the neuron in the *k*th sampling period, ω_{Kjv_1} is refer to $\omega_{\rm Md6\_1}$, $\omega_{\rm Md12\_1}$, $\omega_{\rm Mq6\_1}$, $\omega_{\rm Mq12\_1}$, $\omega_{\rm Bd6\_1}$, $\omega_{\rm Bd12\_1}$, $\omega_{\rm Bq6\_1}$, and $\omega_{\rm Bq12\_1}$, and ω_{Kjv_2} is refer to $\omega_{\rm Md6\_2}$, $\omega_{\rm Md12\_2}$, $\omega_{\rm Mq6\_2}$, $\omega_{\rm Mq12\_2}$, $\omega_{\rm Bd6\_2}$, $\omega_{\rm Bd12\_2}$, $\omega_{\rm Bq6\_2}$, and $\omega_{\rm Bq12\_2}$. μ_2 is the learning rate, e_{Kj} is the difference between the input variable i_{Kj} and the output variable $\hat{i}_{Kj}$ of the ANNBPF, and e_{Kj} is refer to $e_{\rm Md}$, $e_{\rm Mq}$, $e_{\rm Bd}$, and $e_{\rm Bq}$.

Through the ANNBPF as shown in Fig. 5, the amplitude of the same frequency signal as $6\omega_{\rm e}$ and $12\omega_{\rm e}$ in the *d*–*q*-axis currents of torque windings can be extracted. After that 0 can be used as the target command to make difference with the extracted harmonic currents $\hat{i}_{\rm Md}$ and $\hat{i}_{\rm Mq}$, and the compensated control voltages $u_{\rm Mdh}$ and $u_{\rm Mqh}$ can be obtained by adjusting the results

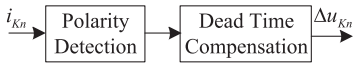

Fig. 6. Block diagram of the DTC control.

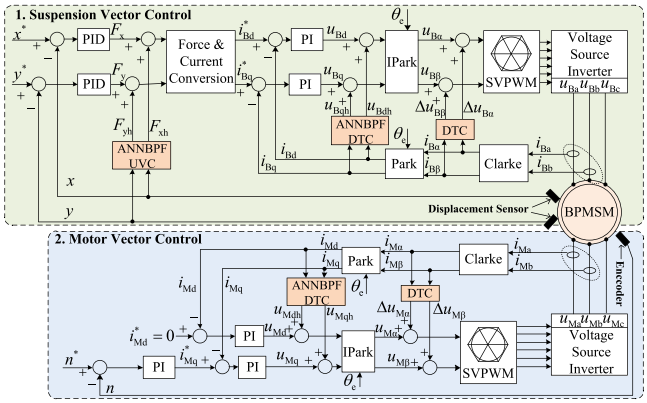

Fig. 7. Block diagram of the BPMSM vibration compensation control.

by PI controller. The implementation in the suspension force windings is similar to the torque windings, and the control block diagram is shown in Fig. 5. The stability proof process is the same as in the previous section, the coefficients of ANNBPF need to be restricted [30]. When the learning rate μ_2 is between 0 and $1/\lambda_{\max 2}$, the stability of the system can be guaranteed, where $\lambda_{\max 2}$ is the maximum value of the matrix eigenvalues, and the matrix is related to $\cos(v\theta_{\mathrm{e}})$ and $\sin(v\theta_{\mathrm{e}})$.

In order to improve the DTC effect for the BPMSM, the DTC method based on current polarity detection is added to the DT voltage compensation method proposed in Section III-B. The advantages of the DTC method for current polarity detection are simple implementation and remarkable effect, but this method has the disadvantage of poor compensation effect at zero current. Hence, the two methods are combined to improve the DTC effect. The current polarity DTC method is mainly implemented by the basic method in [31], and the control block diagram is shown in Fig. 6. By detecting the current polarity of $i_{\mathrm{M}\alpha}$, $i_{\mathrm{M}\beta}$, $i_{\mathrm{B}\alpha}$, and $i_{\mathrm{B}\beta}$, the DTC voltages $\Delta u_{\mathrm{M}\alpha}$, $\Delta u_{\mathrm{M}\beta}$, $\Delta u_{\mathrm{B}\alpha}$, and $\Delta u_{\mathrm{B}\beta}$ are obtained by corresponding compensation methods. In Fig. 6, the subscripts K of i_{Kn} are M and B, the subscripts n denote α and β, i.e., i_{Kn} represents $i_{\mathrm{M}\alpha}$, $i_{\mathrm{M}\beta}$, $i_{\mathrm{B}\alpha}$, and $i_{\mathrm{B}\beta}$, and Δu_{Kn} represents $\Delta u_{\mathrm{M}\alpha}$, $\Delta u_{\mathrm{M}\beta}$, $\Delta u_{\mathrm{B}\alpha}$, and $\Delta u_{\mathrm{B}\beta}$.

C. Overall Structure of the Proposed Control Method

According to the vibration compensation control methods proposed in Sections III-A and III-B, the overall control block diagram of the BPMSM, as shown in Fig. 7, can be constructed.

In Fig. 7, the first part is the suspension force vector control system. In the suspension force vector control system, the outer loop is a displacement control loop, which takes the actual position of the rotor as the target command and obtains the error signal by making a difference with the sampled position signal in the *x*- and *y*-direction. The error signal passes through the PID

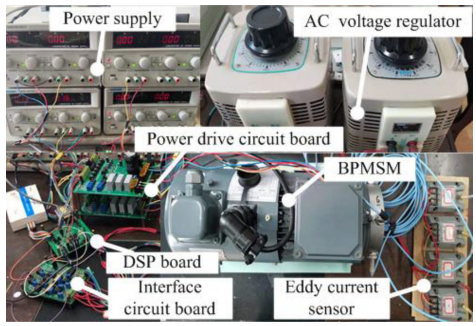

Fig. 8. Schematic diagram of the experimental platform.

controller to obtain F_{x} and F_{y}. F_{xh} and F_{yh} obtained by the unbalanced vibration compensation control algorithm proposed in Fig. 4, and F_{xh} and F_{yh} are added correspondingly with F_{x} and F_{y}, that is, the vibration compensation force is injected into the feedforward channel to complete the unbalanced vibration compensation control. After the force signal is converted by (1), the command currents in the *d*- and *q*-axis are obtained. The error current signals are obtained by subtracting the command currents from the sampled *d*- and *q*-axis current. After the error signals pass through the PI controller, the voltage signals of *d*- and *q*-axis can be obtained. At this time, the proposed ANNBPF DTC algorithm injects the calculated voltage compensation signals u_{Bdh} and u_{Bqh} into the forward channel and add them to u_{Bd} and u_{Bq}. Then, $u_{\mathrm{B}\alpha}$ and $u_{\mathrm{B}\beta}$ are obtained after Ipark transformation. At this time, the DTC algorithm proposed in Fig. 6 is adopted to inject $\Delta u_{\mathrm{B}\alpha}$ and $\Delta u_{\mathrm{B}\beta}$ into the forward channel again and add them together with $u_{\mathrm{B}\alpha}$ and $u_{\mathrm{B}\beta}$. After the SVPWM algorithm, suspension control is carried out. In the motor vector control system, the outer loop is speed loop and the inner loop is current loop. The ANNBPF DTC algorithm proposed in Fig. 5 injects the u_{Mdh} and u_{Mqh} into the forward channel and add them to u_{Md} and u_{Mq}. The added values are transformed by Ipark to obtain $u_{\mathrm{M}\alpha}$ and $u_{\mathrm{M}\beta}$. At this time, the DTC algorithm proposed in Fig. 6 is used to inject the $\Delta u_{\mathrm{M}\alpha}$ and $\Delta u_{\mathrm{M}\beta}$ into the forward channel again and add them to $u_{\mathrm{M}\alpha}$ and $u_{\mathrm{M}\beta}$. After SVPWM algorithm, motor vector control is carried out.

IV. BPMSM Vibration Compensation Control Experiment

In order to verify the effectiveness and correctness of the proposed method, low speed, variable speed, and rated-speed experiments are carried out on the experimental prototype. The experimental prototype is shown in Fig. 8. The parameters of the experimental prototype and power devices are given in Table I. The controller adopts TMS320F28335 and the interrupt frequency is 10 kHz. The vector control algorithm of torque and the control algorithm of suspension are completed in the same interrupt process. In Fig. 8, the upper power drive circuit board supplies power to the torque windings, and the lower power drive circuit board supplies power to the suspension windings. The currents of torque windings and suspension windings are

TABLE I
PARAMETERS OF THE PROTOTYPE AND POWER DEVICES

Symbol	Value	Symbol	Value
U_N (V)	220	δ_0 (mm)	2
P_N (kW)	1.1	ψ_f (Wb)	0.165
n_N (r/min)	3000	L_{Md} / L_{Mq} (mH)	13.42
P_M / P_B	1 / 2	L_{M2} (mH)	2.34
m (kg)	1.6	T_r / T_f (μs)	1.3 / 1.6

TABLE II
PID CONTROLLER PARAMETERS OF VECTOR CONTROL SYSTEM

	Suspension-side		Motor-side	
	Displacement	Current	Speed	Current
K_p	0.2	0.5	240	0.23
K_i	4.6×10^{-4}	4.5×10^{-3}	3.6	1.7×10^{-2}
K_d	1.3×10^{-3}	0	0	0

TABLE III
PARAMETERS OF THE ANNBPF CONTROLLER

	Dead-time part		Unbalanced part
	Suspension-side	Motor-side	
μ_1 / μ_2	0.1 (μ_2)	0.1 (μ_2)	0.1 (μ_1)
K_p	0.23	0.45	0.3
K_i	1.1×10^{-2}	2.0×10^{-3}	2.3×10^{-3}
K_d	0	0	1.3×10^{-3}

collected by Hall current sensor and sent to ADC port of DSP for data acquisition after conditioning by interface circuit board. The real-time position of the rotor is collected by the eddy current sensor, conditioned by the interface circuit board, and sent to the ADC port of DSP for data acquisition. Three ANNBPF algorithms in the proposed method require a total of four sine functions, 50 additions, 60 multiplications, eight PI algorithms, and two PID algorithms. The time consumed is 10 μs, therefore, the real-time performance can meet the control requirements. The PS21965 of Mitsubishi is selected as the power device, and the DT is set to 4 μs. In [26], SiC-based two-level inverters are used to drive the BPMSM. Although the wide bandgap devices can set a smaller DT, the vibration problem caused by the DT effect in general power devices still needs to be studied.

The PID control parameters of vector control system of the BPMSM are given in Table II. The PID parameters of displacement loop and current loop of suspension force windings side and the PID parameters of speed loop and current loop of motor side are given, respectively. The control parameters of the proposed ANNBPF algorithm are given in Table III, in which the ANNBPF parameters of the DT vibration part and the unbalanced vibration part are given, respectively.

First, the experiment without compensation is carried out. Figs. 9–15 show the force and displacement in x- and y-direction, the d- and q-axis current, and the speed waveform, respectively. It can be seen from these figures that at 0–0.5 s, the BPMSM operates at a low speed of 300 r/min and the operating frequency of the BPMSM is 5 Hz. When the BPMSM operates at 300 r/min,

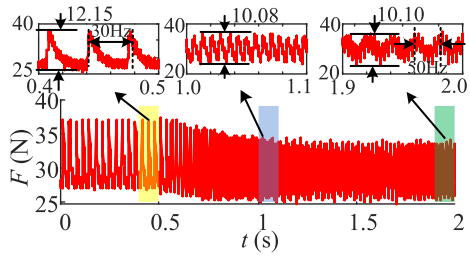

Fig. 9. Waveform of the force in the x-direction without compensation.

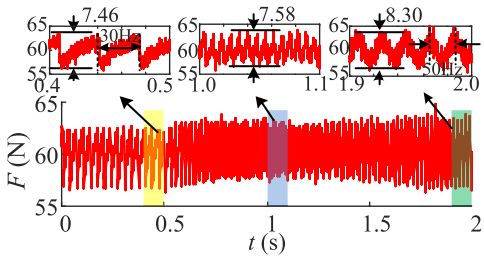

Fig. 10. Waveform of the force in the y-direction without compensation.

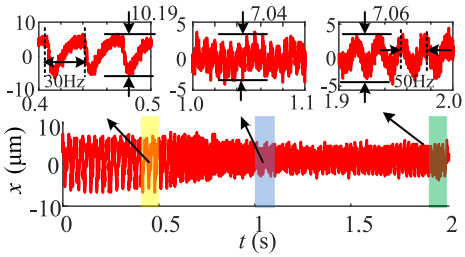

Fig. 11. Waveform of the displacement in the x-direction without compensation.

the main harmonic frequency of the BPMSM is 30 Hz, which is six times the operating frequency. Therefore, the DT effect vibration accounts for the main influencing factor, which is consistent with the previous theoretical analysis. At 0.5–1.83 s, the motor is in acceleration state until it accelerates to 3000 r/min. When the BPMSM is at 3000 r/min, the operating frequency of the BPMSM is 50 Hz, and the main harmonic frequency of the BPMSM is 50 Hz. The operating frequency is consistent with the harmonic frequency. Therefore, unbalanced vibration accounts for the main influencing factor, which is consistent with the previous analysis.

Then, the experiment of the traditional compensation (TRAD COMP) method in [9] is carried out. Figs. 16–22 show the force and displacement in x- and y-direction, the d- and q-axis current, and the speed waveform, respectively. It can be seen from these figures that at 0–0.5 s, the BPMSM runs at a low speed of 300 r/min, and the vibration amplitudes of the force in x- and y-direction are 3.64N and 3.96 N, respectively. The vibration amplitudes of displacement in x- and y-direction are 4.89 and 6.14 μm, respectively. The vibration amplitudes of d- and q-axis currents are 0.21A and 0.22 A, respectively. During

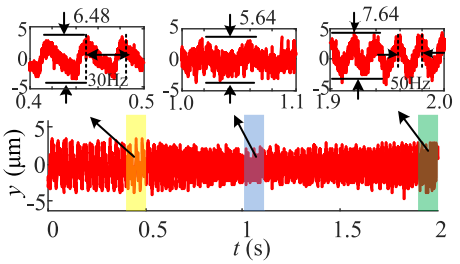

Fig. 12. Waveform of the displacement in the y-direction without compensation.

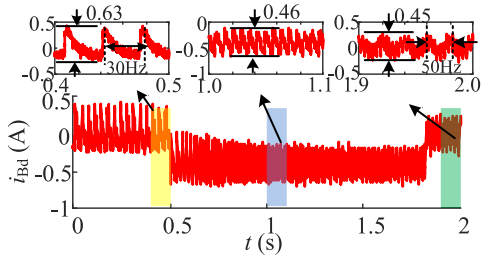

Fig. 13. Waveform of the d-axis current without compensation.

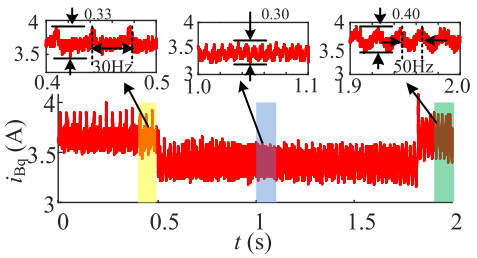

Fig. 14. Waveform of the q-axis current without compensation.

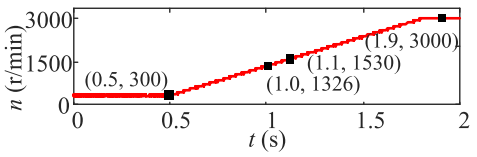

Fig. 15. Waveform of the speed without compensation.

0.5–1.83 s, the BPMSM is in the acceleration state. At 1.0–1.1 s, the vibration amplitudes of the force in x- and y-direction are 3.58 and 3.95 N, respectively. The vibration amplitudes of displacement in x- and y-direction are 4.95 and 5.08 μm, respectively. The vibration amplitudes of d- and q-axis currents are 0.22 and 0.25 A, respectively. The BPMSM maintains the operation of 3000 r/min after the acceleration is completed. During this period, the vibration amplitudes of the force in x- and y-direction are 4.25 and 5.13 N, respectively. The vibration amplitudes of displacement in x- and y-direction are 5.76 and 6.02 μm, respectively. The vibration amplitudes of d- and q-axis currents are 0.37 and 0.3 5 A, respectively.

Finally, the experiment of the proposed compensation (PPSD COMP) method is carried out. Figs. 23–29 show the force and

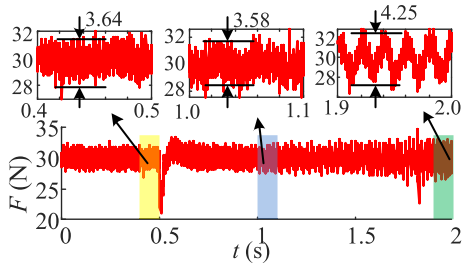

Fig. 16. Waveform of the force in the x-direction with TRAD COMP.

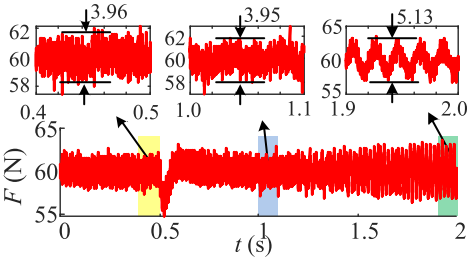

Fig. 17. Waveform of the force in the y-direction with TRAD COMP.

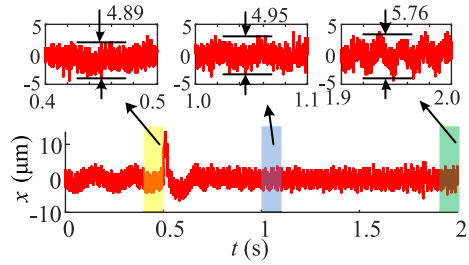

Fig. 18. Waveform of the displacement in the x-direction with TRAD COMP.

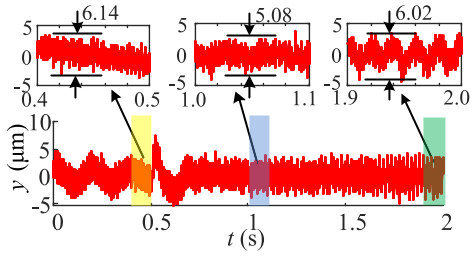

Fig. 19. Waveform of the displacement in the y-direction with TRAD COMP.

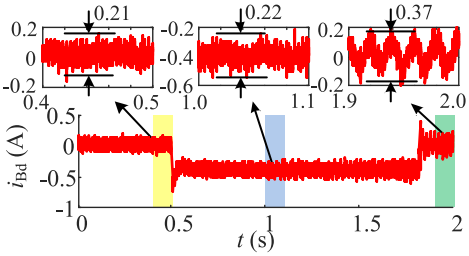

Fig. 20. Waveform of the d-axis current with TRAD COMP.

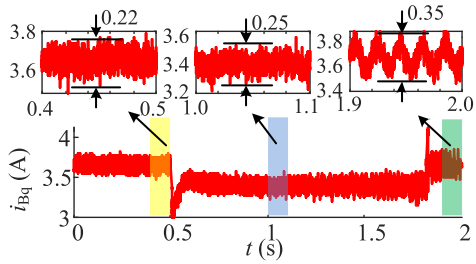

Fig. 21. Waveform of the q-axis current with TRAD COMP.

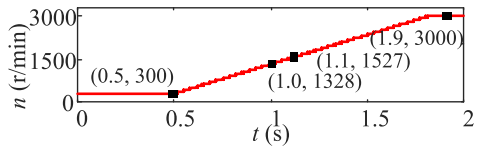

Fig. 22. Waveform of the speed with TRAD COMP.

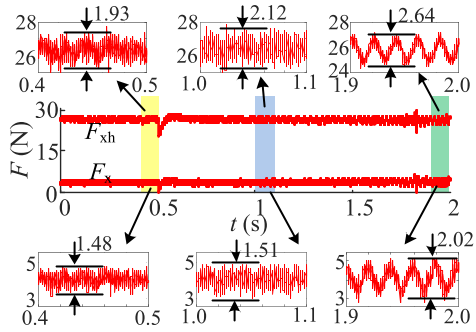

Fig. 23. Waveform of the force in the x-direction with PPSD COMP.

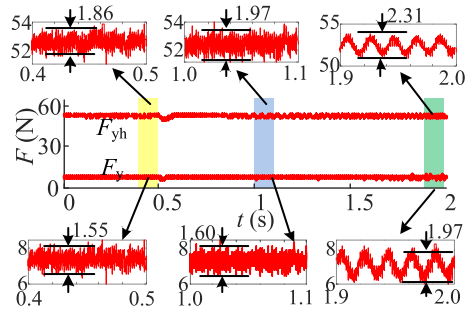

Fig. 24. Waveform of the force in the y-direction with PPSD COMP.

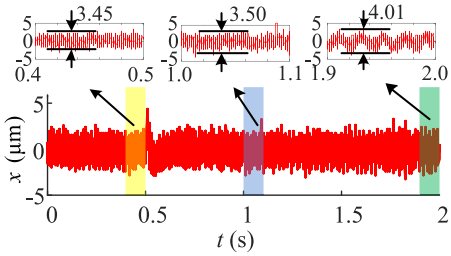

Fig. 25. Waveform of the displacement in the x-direction with PPSD COMP.

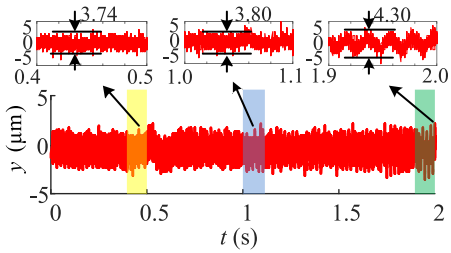

Fig. 26. Waveform of the displacement in the y-direction with PPSD COMP.

displacement in x- and y-direction, the d- and q-axis current, and the speed waveform, respectively. It can be seen from these figures that at 0–0.5 s, the BPMSM operates at a low speed of 300 r/min, and the vibration amplitudes of the force in x- and y-direction are 1.48 and 1.55 N, respectively. Compared with the TRAD COMP control method, the vibration amplitudes are reduced by 46.97% and 53.03%, respectively. The vibration amplitudes of the displacement in x- and y-direction are 3.45 and 3.74 μm, respectively. Compared with the TRAD COMP control method, the vibration amplitudes are reduced by 29.45% and 39.09%, respectively. The vibration amplitudes of d- and q-axis currents are 0.18 and 0.18 A, respectively. Compared with the TRAD COMP control method, the vibration amplitudes are reduced by 14.29% and 18.18%, respectively. During 0.5–1.83 s, the BPMSM is in the acceleration state. At 1.0–1.1 s, the vibration amplitudes of the force in x- and y-direction are 1.51 and 1.60 N, respectively. Compared with the TRAD COMP control method, the vibration amplitudes are reduced by 40.78% and 50.13%, respectively. The vibration amplitudes of the displacement in x- and y-direction are 3.50 and 3.80 μm, respectively. Compared with the TRAD COMP control method, the vibration amplitudes are reduced by 29.29% and 25.20%, respectively. The vibration amplitudes of d- and q-axis currents are 0.21 and 0.22 A, respectively. Compared with the TRAD COMP control method, the vibration amplitudes are reduced by 4.55% and 12.00%, respectively. After the acceleration of the BPMSM is completed, it is maintained at 3000 r/min. During this period, the vibration amplitudes of the force in x- and y-direction are 2.02 and 1.97 N, respectively. Compared with the TRAD COMP control method, the vibration amplitudes are reduced by 37.88% and 54.97%, respectively. The vibration amplitudes of the displacement in x- and y-direction are 4.01 and 4.30 μm, respectively. Compared with the TRAD COMP control method, the vibration amplitudes are reduced by 30.38% and 28.57%, respectively. The vibration amplitudes of d-axis and q-axis currents are 0.35 and 0.29 A, respectively. Compared with the TRAD COMP control method, the vibration amplitudes are reduced by 5.41% and 17.14%, respectively.

According to the previous analysis, the vibration force of the BPMSM is related to the mechanical angular velocity and the electrical angular velocity. When the BPMSM runs at low speed and rated speed, respectively, the vibration force in the x- and y-direction is affected by unbalanced vibration and DT effect vibration. Through the FFT analysis of the force in the x- and

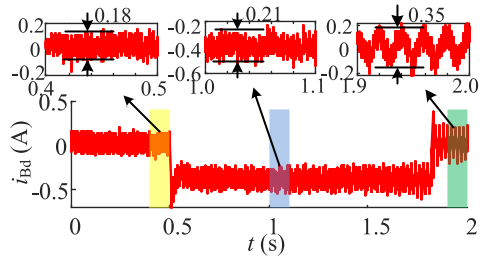

Fig. 27. Waveform of the d-axis current with PPSD COMP.

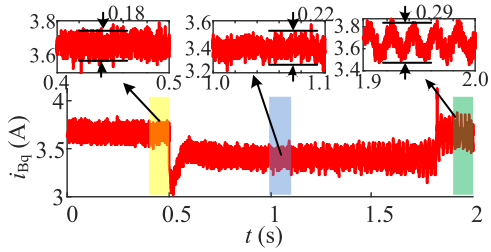

Fig. 28. Waveform of the q-axis current with PPSD COMP.

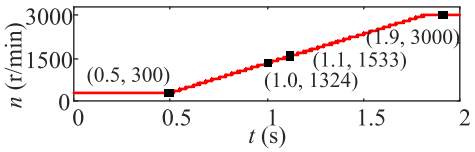

Fig. 29. Waveform of the speed with PPSD COMP.

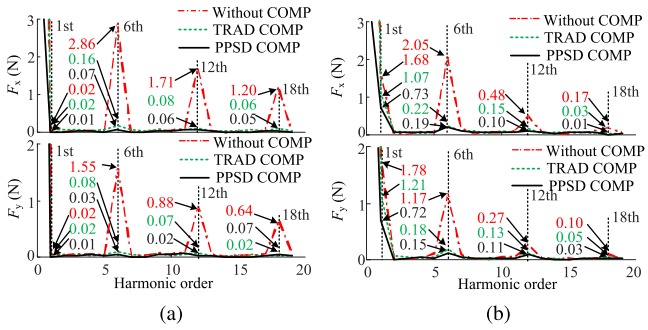

Fig. 30. Harmonic amplitude of radial force at low and rated speeds. (a) Low speed. (b) Rated speed.

y-direction, the spectrum of F_x and F_y, as shown in Fig. 30(a) and (b), can be obtained. At this time, the fundamental frequency of Fig. 30(a) is 5 Hz and the fundamental frequency of Fig. 30(b) is 50 Hz. In the absence of vibration compensation, the amplitudes of the 6th and 12th harmonics of F_x at low-speed operation are 2.86 and 1.71 N, respectively, and the amplitudes of the 6th and 12th of F_x at rated-speed operation are 2.05 and 0.48 N, respectively. After TRAD COMP, the amplitudes of the 6th and 12th harmonics of F_x are reduced to 0.16 and 0.08 N at low speed and 0.0222 and 0.15 N at rated speed. After PPSD COMP, the amplitudes of the 6th and 12th harmonics of F_x are reduced to 0.07 and 0.06 at low speed and 0.19 and 0.10 N at rated speed. The amplitude of the first order harmonic of F_x is only 0.02 N at low speed without vibration compensation, however, 1.68 N at rated speed. After TRAD COMP, the vibration amplitude is reduced to 0.02 N at low speed and 1.07 N at rated speed. While after PPSD COMP, the vibration amplitude is reduced to 0.01 N at low speed and 0.73 N at rated speed. It can be seen that the unbalanced vibration will gradually appear at a rated speed and the vibration amplitude is small at low speed, which can be ignored, and the PPSD COMP method can better suppress the unbalanced vibration than TRAD COMP of the rotor.

In the absence of vibration compensation, the variation law of the amplitude of F_y at low speed and rated speed is the same as that of F_x.

By comparing Fig. 30(a) with (b), it can be seen that in rated-speed operation, even if the vibration compensation control is not carried out, the amplitude of the 6th and 12th harmonic of the vibration force will also be reduced. This is due to the speed increases, the motor impedance will increase correspondingly. According to (7), the amplitude of the vibration force will also decrease correspondingly. In the analysis process, the influence of higher harmonics is ignored, and only the 6th and 12th harmonics are analyzed, but the 18th harmonic component and higher (24th, 30th, $\cdots$) harmonic components also exist.

V. Conclusion

In this article, a vibration compensation control method based on ANNBPF was proposed to solve the problem of rotor vibration of the BPMSM. Previous studies on rotor vibration only considered the factors of rotor unbalanced vibration, but lacked research on other vibration reasons. In fact, the rotor vibration of the BPMSM is not only related to the unbalance mass but also related to the DT effect. Therefore, the rotor vibration includes the unbalanced vibration and the DT vibration. Moreover, the frequency of unbalanced vibration is related to the rotor mechanical angular velocity, and the frequency of DT vibration is related to the rotor electrical angular velocity. The experimental results demonstrated that when the BPMSM ran at low speed, the amplitude of unbalanced vibration accounted for a small proportion, and the DT vibration was the main cause of rotor vibration. However, when the BPMSM ran at rated speed, the amplitude of DT vibration decreases with the increase of speed, and the unbalanced vibration will become the dominant factor of rotor vibration. Through the proposed vibration compensation control algorithm, the problem of rotor vibration of the BPMSM can be effectively suppressed. In the future work, more factors related to vibration will be explored and theoretical analysis and compensation control research will be carried out. A simpler and more effective vibration compensation control algorithm will also be studied.

References

[1] J. Chen, J. Zhu, and E. L. Severson, "Review of bearingless motor technology for significant power applications," *IEEE Trans. Ind. Appl.*, vol. 56, no. 2, pp. 1377–1388, Mar./Apr. 2020.

[2] Y. Fu, M. Takemoto, S. Ogasawara, and K. Orikawa, "Investigation of operational characteristics and efficiency enhancement of an ultrahigh-speed bearingless motor at 100 000 r/min," *IEEE Trans. Ind. Appl.*, vol. 56, no. 4, pp. 3571–3583, Jul./Aug. 2020.
[3] G. Valente, A. Formentini, L. Papini, C. Gerada, and P. Zanchetta, "Performance improvement of bearingless multisector PMSM with optimal robust position control," *IEEE Trans. Power Electron.*, vol. 34, no. 4, pp. 3575–3585, Apr. 2019.
[4] Y. Hua, H. Zhu, M. Gao, and Z. Ji, "Multiobjective optimization design of permanent magnet assisted bearingless synchronous reluctance motor using NSGA-II," *IEEE Trans. Ind. Electron.*, vol. 68, no. 11, pp. 10477–10487, Nov. 2021.
[5] J. Asama, T. Shibata, T. Oiwa, T. Shinshi, and A. Chiba, "Performance improvement of a bearingless motor by rotation about an estimated center of inertia," in *Proc. 11th Int. Symp. Linear Drives Ind. Appl.*, 2019, pp. 1–5.
[6] W. Bu, F. He, C. Lu, Z. Li, and J. Xiao, "Unbalanced vibration control strategy of bearingless induction motor based on inverse system decoupling," *Int. J. Appl. Electromagn. Mech.*, vol. 51, no. 4, pp. 455–469, Aug. 2016.
[7] W. Bu, Y. Huang, C. Lu, H. Zhang, and H. Shi, "Unbalanced displacement LMS extraction algorithm and vibration control of a bearingless induction motor," *Int. J. Appl. Electromagn. Mech.*, vol. 56, no. 1, pp. 35–47, Dec. 2018.
[8] W. Bu, X. Tu, C. Lu, and Y. Pu, "Adaptive feedforward vibration compensation control strategy of bearingless induction motor," *Int. J. Appl. Electromagn. Mech.*, vol. 63, no. 2, pp. 199–215, Jun. 2020.
[9] H. Zhu, Z. Yang, X. Sun, D. Wang, and X. Shen, "Rotor vibration control of a bearingless induction motor based on unbalanced force feedforward compensation and current compensation," *IEEE Access*, vol. 8, pp. 12988–12998, 2020.
[10] C. Tan, H. Wang, and Y. Wang, "Rotor eccentricity compensation of bearingless switched reluctance motors based on extended Kalman filter," in *Proc. 12th Int. Symp. Comput. Intell. Des.*, 2019, pp. 111–115.
[11] J. Fei, H. Wang, and Y. Fang, "Novel neural network fractional-order sliding-mode control with application to active power filter," *IEEE Trans. Syst. Man Cybern.: Syst.*, to be published, doi: 10.1109/TSMC.2021.3071360.
[12] J. Fei, Z. Wang, X. Liang, Z. Feng, and Y. Xue, "Fractional sliding mode control for micro gyroscope based on multilayer recurrent fuzzy neural network," *IEEE Trans. Fuzzy Syst.*, to be published, doi: 0.1109/TFUZZ.2021.3064704.
[13] J. Fei, Y. Chen, L. Liu, and Y. Fang, "Fuzzy multiple hidden layer recurrent neural control of nonlinear system using terminal sliding-mode controller," *IEEE Trans. Cybern.*, to be published, doi: 10.1109/TCYB.2021.3052234.
[14] Z. Wang and J. Fei, "Fractional-order terminal sliding mode control using self-evolving recurrent Chebyshev fuzzy neural network for MEMS gyroscope," *IEEE Trans. Fuzzy Syst.*, to be published, doi: 10.1109/TFUZZ.2021.3094717.
[15] T. Reichert, T. Nussbaumer, and J. W. Kolar, "Bearingless 300-W PMSM for bioreactor mixing," *IEEE Trans. Ind. Electron.*, vol. 59, no. 3, pp. 1376–1388, Mar. 2012.
[16] T. Wellerdieck, T. Nussbaumer, and J. W. Kolar, "Angle-sensorless zero- and low-speed control of bearingless machines," *IEEE Trans. Magn.*, vol. 52, no. 7, pp. 1–4, Jul. 2016.
[17] Z. Tang and B. Akin, "Suppression of dead-time distortion through revised repetitive controller in PMSM drives," *IEEE Trans. Energy Convers.*, vol. 32, no. 3, pp. 918–930, Sep. 2017.
[18] Z. Tang and B. Akin, "A new LMS algorithm based deadtime compensation method for PMSM FOC drives," *IEEE Trans. Ind. Appl.*, vol. 54, no. 6, pp. 6472–6484, Nov./Dec. 2018.
[19] T. Qiu, X. Wen, and F. Zhao, "Adaptive-linear-neuron-based dead-time effects compensation scheme for PMSM drives," *IEEE Trans. Power Electron.*, vol. 31, no. 3, pp. 2530–2538, Mar. 2016.
[20] K. Liu and Z. Q. Zhu, "Online estimation of rotor flux linkage and voltage source inverter nonlinearity in permanent magnet synchronous machine drives," *IEEE Trans. Power Electron.*, vol. 29, no. 1, pp. 418–427, Jan. 2013.
[21] L. Wang, Z. Zhu, H. Bin, and L. M. Gong, "Current harmonics suppression strategy for PMSM with non-sinusoidal back-EMF based on adaptive linear neuron method," *IEEE Trans. Ind. Electron.*, vol. 67, no. 11, pp. 9164–9173, Nov. 2019.
[22] Y. Zhao, W. Qiao, and L. Wu, "Dead-time effect analysis and compensation for a sliding-mode position observer-based sensorless IPMSM control system," *IEEE Trans. Ind. Appl.*, vol. 51, no. 3, pp. 2528–2535, May/Jun. 2015.
[23] D. Wang, M. Wang, Y. Shen, Q. Li, and X. Liang, "Online feedback dead time compensation strategy for three-level T-type inverters," *IEEE Trans. Ind. Electron.*, vol. 67, no. 9, pp. 7260–7268, Sep. 2020.
[24] X. Sun, L. Chen, H. Jiang, Z. Yang, J. Chen, and W. Zhang, "High-performance control for a bearingless permanent-magnet synchronous motor using neural network inverse scheme plus internal model controllers," *IEEE Trans. Ind. Electron.*, vol. 63, no. 6, pp. 3479–3488, Jun. 2016.
[25] Y. Hua and H. Zhu, "Rotor radial displacement sensorless control of bearingless permanent magnet synchronous motor based on MRAS and suspension force compensation," *ISA Trans.*, vol. 103, pp. 306–318, Aug. 2020.
[26] Y. Jiang, R. A. Torres, and E. L. Severson, "Current regulation in parallel combined winding bearingless motors," *IEEE Trans. Ind. Appl.*, vol. 55, no. 5, pp. 4800–4810, Sep./Oct. 2019.
[27] H. Zhu and J. Huang, "Compensation control of suspension force for LS-BLPMSM," *Inst. Eng. Technol. Electr. Power Appl.*, vol. 11, no. 4, pp. 622–630, Apr. 2017.
[28] Z. Qiu, J. Dai, J. Yang, X. Zhou, and Y. Zhang, "Research on rotor eccentricity compensation control for bearingless surface-mounted permanent-magnet motors based on an exact analytical method," *IEEE Trans. Magn.*, vol. 51, no. 11, pp. 1–4, Nov. 2015.
[29] Z. Wu *et al.*, "Dead-time compensation based on a modified multiple complex coefficient filter for permanent magnet synchronous machine drives," *IEEE Trans. Power Electron.*, vol. 36, no. 11, pp. 12979–12989, May 2021.
[30] K. Liu and Z. Q. Zhu, "Position-offset-based parameter estimation using the adaline NN for condition monitoring of permanent-magnet synchronous machines," *IEEE Trans. Ind. Electron.*, vol. 62, no. 4, pp. 2372–2383, Apr. 2015.
[31] D. Wang, B. Yang, C. Zhu, Z. Chuanwei, and Q. Ji, "A feedback-type phase voltage compensation strategy based on phase current reconstruction for ACIM drives," *IEEE Trans. Power Electron.*, vol. 29, no. 9, pp. 5031–5043, Sep. 2014.

Xin Wang was born in Jiangsu, China, in 1993. He received the M.S. degree in mechanical engineering from the Jiangsu University of Technology, Changzhou, China, in 2019. He is currently working toward the Ph.D. degree in electrical engineering with Jiangsu University, Zhenjiang, China.

His research interests include optimal design of bearingless permanent magnet synchronous motor and drive control of bearingless permanent magnet synchronous motor.

Huangqiu Zhu (Member, IEEE) received the B.S. degree in automation from the School of Electrical and Information Engineering and the M.S. degree in management from Jiangsu University, Zhenjiang, China, in 1987 and 1993, respectively, and the Ph.D. degree from Nanjing University and Aeronautics and Astronautics, Nanjing, China, in 2000.

From 2002 to 2003, he was a Visiting Scholar with the Swiss Federal Institute of Technology, Zurich, Switzerland. He is currently a Professor with the Department of Electrical Engineering, Jiangsu University. His research interests include magnetic bearings, magnetic suspension (bearingless) motors, and motors and movement control.